Discrete particle simulations of high pressure fluidization

W. Godlieb, N.G. Deen*, J.A.M. Kuipers
University of Twente, Faculty of Science and Technology,
P.O. Box 217, NL-7500 AE Enschede, The Netherlands;
* Corresponding author, Tel. +31 53 489 4138, Fax +31 53 489 2882, E-mail:
N.G.Deen@utwente.nl

Abstract

Low density polyethylene and polypropylene are produced at large scale via the Unipol process. In this process catalyst particles are fluidized with monomer gas which reacts with the catalyst particles to form polymeric particles up to a size of 1 mm. The process is typically operated at pressures of 20 to 25 bar. Pressure impacts the hydrodynamics of the fluidized bed as it influences the bubble behaviour, particle mixing and heat transfer characteristics. Despite decades of research on fluid beds these effects are not completely understood.

In order to gain more insight in the effects of operating pressure on the fluidization behaviour we have performed full 3D discrete particle simulations. We use a state-of-the art discrete particle model (DPM) to simulate fluidization behaviour at different pressures. In our model the gas phase is described by the volume-averaged Navier-Stokes equations, whereas the particles are described by the Newtonian equations of motion. The DPM accurately accounts for the gas-particle interaction, which is necessary for capturing the pressure effect.

The simulation results were analysed with spectral analysis of the pressure drop fluctuations and analysis of the porosity field. In order to study the bubble behaviour, a sophisticated bubble detection algorithm was developed. From this algorithm, gas bubble characteristics, such as bubble velocity and bubble size are obtained.

The simulation results show increasing emulsion porosity and decreasing bubble porosity with increasing pressure. In other words, the bubble-emulsion structure becomes less distinct. The determined bubble velocity is very well in accordance with empirical correlations for low pressures, and decreases at elevated pressures.

Keywords: high pressure fluidization, fluidized bed, discrete particle model, bubble detection algorithm.

Introduction

Polyethylene is the plastic with the highest production capacity in the world, which is a result of the availability of a flexible and efficient fluidized-bed-based technology using a fine catalyst. Despite decades of research, this process is not sufficiently well understood.

Especially important is the impact of pressure on gas bubbles behaviour since many unique properties of the bed can be directly related to the presence of bubbles. The objective of this work is to gain insight in the fluidization behaviour of the polyethylene particles at elevated pressure, using sophisticated state-of-the-art CFD models. Several groups have reported experimental investigations of pressurized fluidized beds such as Olowson & Almstedt (1990), Chan et al. (1987), Olowson & Almstedt (1990, (1991, (1992), Chitester et al. (1984; Sidorenko & Rhodes (2004; Wiman & Almstedt (1998). They reported various pressure-dependent relations for drag, bubble properties, minimum fluidization velocity, and minimum bubbling velocity. Only recently detailed computational models have been used to study pressurized fluidized beds. Li & Kuipers (2005) performed 2D discrete particle simulations

and found a less distinct bubble-emulsion structure and gave a qualitative explanation of this effect. Bokkers et al. (2004) and Laverman (2006) performed several discrete bubble simulations for a large scale polyethylene fluid bed, but assumed atmospheric conditions. In these simulations closure information on the bubble and emulsion properties is crucial for a reliable model prediction. More detailed DPM simulations could in principle provide this information.
In this work we performed discrete particle simulations to obtain qualitative and quantitative knowledge on pressure dependence of fluid bed properties. Contrary to the work of Li & Kuipers (2005), the simulations are carried out in full 3D employing a sufficiently large calculation domain.
This paper is organized as follows: first the theoretical background of the DPM and the applied analysis techniques are outlined. Subsequently, the results of full 3D simulations at different operating pressures are presented. Finally the results are discussed in detail and conclusions are presented.

Governing Equations

The discrete particle model (DPM) is an Euler-Lagrange model, which was originally developed by Hoomans et al. (1996). In the DPM every particle is individually tracked accounting for particle-particle and particle-wall collisions.

In the DPM the gas phase hydrodynamics are described by the Navier-Stokes equations:

$$\frac{\partial}{\partial t}(\varepsilon_g \rho_g) + \nabla \cdot (\varepsilon_g \rho_g \bar{u}_g) = 0 \tag{1}$$

$$\frac{\partial}{\partial t}(\varepsilon_g \rho_g \bar{u}_g) + \nabla \cdot (\varepsilon_g \rho_g \bar{u}_g \bar{u}_g) = -\varepsilon_g \nabla \rho_g - \nabla \cdot (\varepsilon_g \bar{\bar{\tau}}_g) - \bar{S}_p + \varepsilon_g \rho_g \bar{g}$$

where $\bar{u}_g$ is the gas velocity and $\bar{\bar{\tau}}_g$ represents the gas phase stress tensor. The sink term $\bar{S}_p$, represents the drag force exerted on the particles:

$$\bar{S}_p = \frac{1}{V_{cell}} \int_{V_{cell}} \sum_{i=0}^{Npart} \frac{V_i \beta}{1-\varepsilon_g} \left(\bar{u}_g - \bar{v}_i\right) D\left(\bar{r} - \bar{r}_i\right) dV \tag{2}$$

The distribution function $D\left(\bar{r} - \bar{r}_i\right)$ is a discrete representation of a Dirac delta function that distributes the reaction force acting on the gas to the Eulerian grid via a volume-weighing technique. The inter-phase momentum transfer coefficient, β describes the drag of the gas-phase acting on the particles. The Ergun (1952) and Wen & Yu (1966) equations are commonly used to obtain expressions for β. However, we use the closure relation derived by Koch & Hill (2001) based on lattice Boltzmann simulations, since it has no discontinuities at high Reynolds numbers and gives good results as reported by Link et al. (2005).
The motion of every individual particle i in the system is calculated from Newtons's law:

$$m_i \frac{d\bar{v}_i}{dt} = -V_i \nabla p + \frac{V_i \beta}{\varepsilon_s}\left(\bar{u} - \bar{v}_i\right) + m_i \bar{g} + F_i^{pp} + F_i^{pw} \tag{3}$$

where the forces on the right hand side are, respectively due pressure, drag, gravity, particle-particle interaction and particle-wall interaction.

The contact forces are caused by collisions with other particles or confining walls. These collisions are described with a soft-sphere approach. This approach uses a linear spring/dash-pot model, wherein the velocities, positions and collision forces of the particles are calculated at every fixed time step via a first order time integration (Hoomans et al. (1996)). The collision model takes restitution and friction effects into account. The associated collision coefficients were obtained experimentally via the method of Kharaz et al. (1999). They developed a sophisticated experimental method to obtain collision parameters for different impact angles. For more details on the implementation of the soft-sphere model we refer to the work of Ye et al. (2005).

Bubble detection algorithm

The effect of bubbles on fluidized bed hydrodynamics and performance has been studied extensively in literature. Since the bubbles are responsible for the mixing in a fluidized bed, many important bubble properties, such as rise velocity, size, shape and wake size have been determined experimentally. The formation of heterogeneous structures such as bubbles is a direct outcome of the discrete particle simulation. In order to detect these structures, enabling subsequent analysis and direct comparison with experimental data, a bubble detection algorithm is required. In this study we report an algorithm that can distinguish bubbles from the emulsion phase. The algorithm essentially consists of three steps: calculation of the porosity field, determination a threshold value and correlation of detected bubbles. First we calculate the porosity for each computational cell, by subtracting the volume of the particle from the volume associated with that cell. Small clusters of particles disturb the detection, causing small 'holes' in the bubbles and difficulties in detecting the bubble edge. Therefore we smooth the porosity plot by applying a moving average filter with a size of 3x3x3 cells.
In the second step a threshold value for the porosity is determined. In order to identify bubbles of varying porosity a variable threshold value was used. Areas with a porosity above the threshold value are attributed to the bubbles, whereas the remainder of the cells are attributed to the emulsion phase. The threshold value is determined as follows.

$$\varepsilon_{th} = \min(\max(\varepsilon_{min}, e_{loc}), \varepsilon_{max}) \tag{4}$$

where $\varepsilon_{min} = 0.6$ and $\varepsilon_{max} = 0.8$ are the minimum and maximum threshold values respectively and ε_{loc} is the local porosity of the emulsion phase. which is calculated as:

$$\varepsilon_{loc} = \max(\varepsilon(i,j,k) - 0.2 \;\forall (i-5) < x < (i+5), (j-5) < y < (j+5), (k-5) < z < (k+5) \tag{5}$$

where (i,j,k) are the indices of the applied grid cells. The numerical values used for determining the threshold were found to give the best accordance between visual detection and the detection results. To prevent grid size dependency, after ε_{loc} has been obtained for each grid cell a moving average filter of 10x10x10 cells is applied.

Figure 1: Snapshots showing intermediate results of the bubble detection algorithm: a) the particle positions; b) porosity of the bed; c) smoothed porosity; d) threshold value; e) smoothed threshold value; f) bubble detection results; g) equivalent bubble diameter.

After all cells haven been identified all bubble cells which are connected to each other are attributed to the same bubble. The bubble position, i.e. the centre of mass and equivalent bubble radius can be easily calculated from the average cell position and number of cells pertaining to the bubble, respectively.
In the third and final step of the bubble detection algorithm two subsequent detection results are correlated. Bubbles in two subsequent bubble maps that are less than one bubble radius apart, are considered to constitute the same bubble. From the bubble displacement between two subsequent detection results the bubble velocity can be calculated. If coalescence or break-up occurs, the involved bubbles will move more than one bubble radius, and the bubble positions are discarded in the velocity calculation. For practical purposes the relative bubble velocity, i.e. the slip velocity is much more relevant than the absolute bubble velocity. To this end we also need the emulsion velocity, which is calculated by averaging the velocity of all the particles in the first computational cell around the bubble. The slip velocity is subsequently calculated as:

$$v_\infty = v_b - v_e \tag{6}$$

where v_b and v_e are the velocities of the bubble and the surrounding emulsion phase respectively.

Spectral analysis of pressure fluctuations

Gas flows more easily through the bubbles compared to the emulsion; leading to a lower pressure inside the bubbles. Due to the continuous passage of bubbles through the fluidized bed, the pressure drop measured over the bed height is continuously fluctuating. Link et al. (2005) designed a method to apply spectral analysis to DPM results. By recording the pressure drop over the bed as a function of time and applying a Fourier transformation to the pressure signal, they were able to determine the main pressure fluctuation frequency. In the

simulations the pressure is averaged over the top and the bottom planes of the bed every 4 ms. Subsequently a Fourier transformation over 2048 data points, was performed using Microsoft Excel.

Results

To investigate the pressure effect on several fluidization properties four full 3D DPM simulations at 2, 4, 8 and 16 bar were performed. The system properties and operating conditions are specified in Table 1 and Table 2, respectively.

Property	symbol	value	unit	
system width	X	0.025	m	(20 cells)
system depth	Y	0.025	m	(20 cells)
system height	Z	0.1	m	(80 cells)
time step	dt	$1.0 \cdot 10^{-4}$	s	
total time	t	10	s	
number of particles	N_{part}	$2.86 \cdot 10^{5}$	-	
particle diameter	r_p	5.0	mm	
spring stiffness	k_n	200	N/m	
coefficient of normal restitution	e_n	0.8	-	
coefficient of tangential restitution	e_t	0.6	-	
particle density	ρ	925	kg/m^3	
friction coefficient	μ	0.1	-	

Table 1: Settings for all four simulations.

The coefficients of restitution and the friction coefficients used in the simulations were measured according to the method described by Kharaz et al. (1999).

No-slip boundary conditions were used at the walls.
In order to enable a fair comparison between the simulations, a constant excess velocity (i.e. superficial gas velocity minus minimum fluidisation velocity) of 0.177 m/s was applied.

In this section we will discuss the results of these simulations, where we will focus on porosity distributions, bubble size and velocity distributions and pressure drop fluctuation spectra.

P (bar)	u_{mf} (m/s)	u_{gas} (m/s)
2	0.084	0.261
4	0.077	0.253
8	0.067	0.244
16	0.056	0.233

Table 2: Superficial gas velocities for the 3D simulations.

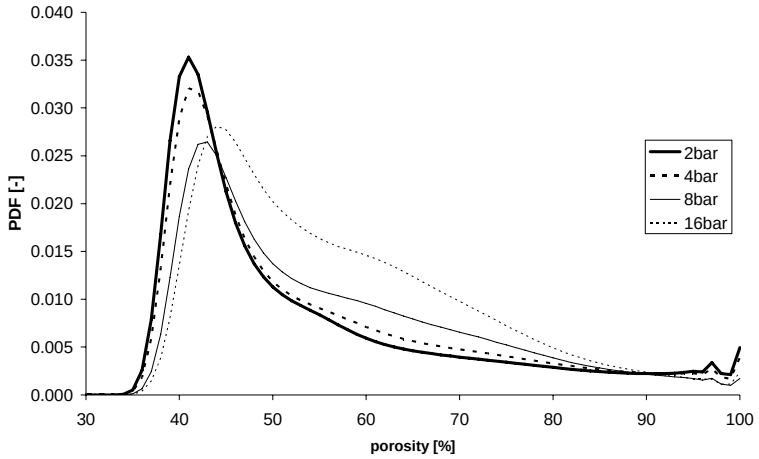

Figure 2: PDF of time-averaged porosity distribution at 2, 4, 8 and 16 bar.

The PDF of the time-averaged porosity distributions resulting from the simulations are shown in Figure 2. Only the dense zone of the bed is taken into account.
Around a porosity of 40% - 45% we see a clear peak representing the emulsion phase. Notice that at maximum packing the porosity is about 26%. Above 95% we see some small peaks caused by bubbles. An intermediate area with porosities between 45% and 90% is located around bubbles or in developing or collapsing bubbles.
It is very clear that the emulsion phase becomes less dense with increasing pressure, as the peak moves from 40% at 2 bar to 45% at 16 bar. Furthermore it can be observed that the intermediate region becomes more dominant with increasing pressure.

Similar to Figure 2 a PDF of the bubble porosity distribution is presented in Figure 3. However in this case only the cells that are attributed to the bubbles are taken into account. It can be clearly observed that the bubble porosity decreases with increasing pressure, i.e. the bubbles contain more particles.
Summarizing, it is found that with increasing pressure the emulsion phase becomes less dense, while the bubbles become more dense. Consequently the bubbles and the emulsion phase become less distinct.

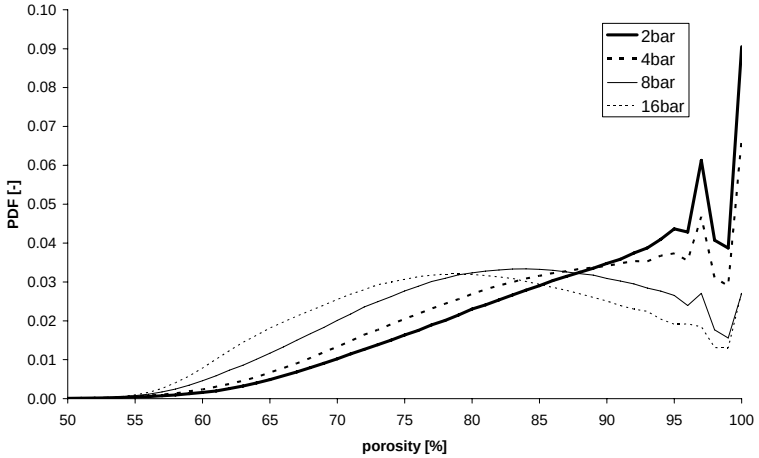

Figure 3: PDF of time-averaged bubble porosity distribution at 2, 4, 8 and 16 bar. Only the cells attributed to the bubbles are taken into account.

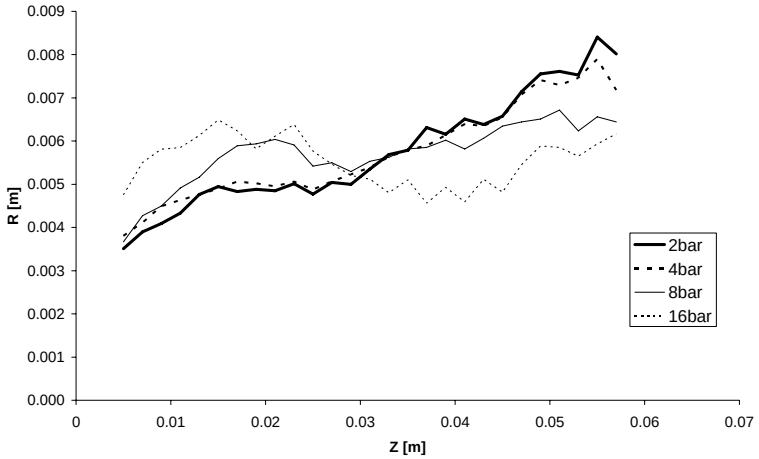

Figure 4: Equivalent bubble radius, calculated by bubble detection algorithm, as a function of bed height.

In Figure 4 the average bubble size versus the bed height is shown. At low pressure we see a continuously increasing bubble size caused by bubble growth and coalescence. At higher pressures however a more stable average bubble size is observed.

In Figure 5 snapshots of the particle positions at different operating pressures are shown. A distinctly different bubble behaviour can be discerned from this figure. At elevated pressures the bubbles tend to be smaller. Furthermore the porosity distribution becomes more homogeneous, as was observed before.

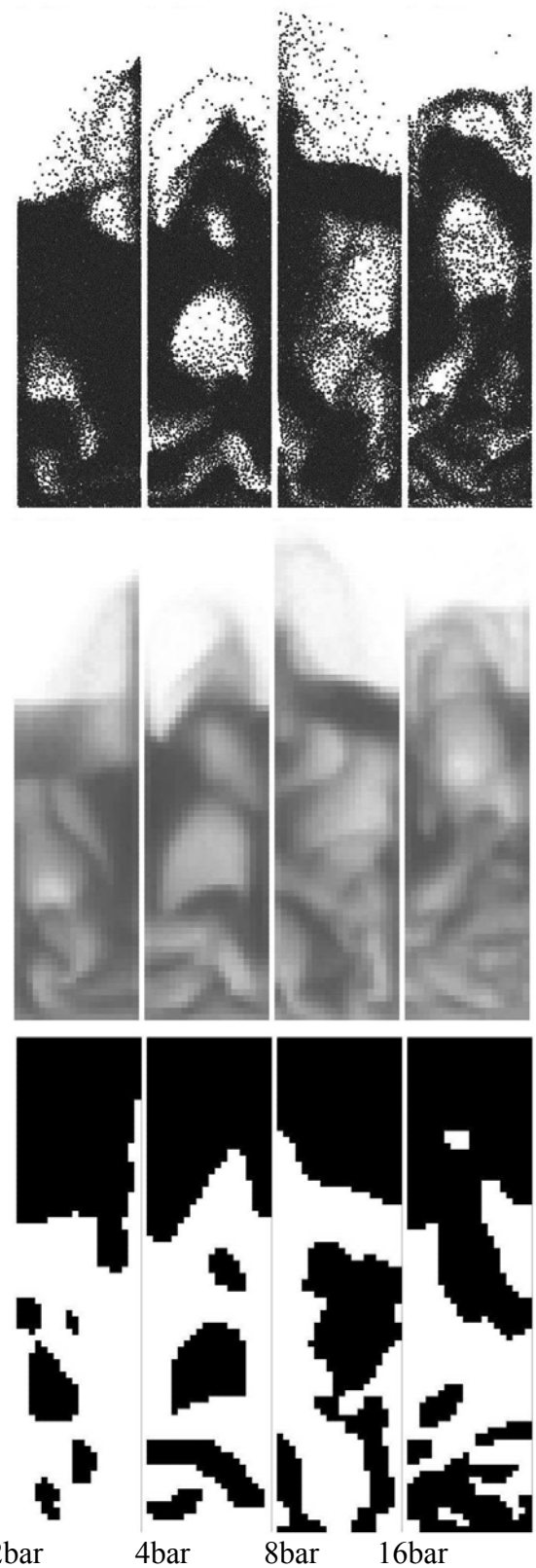

Figure 5: Bubble detection results. **Top row:** Snapshots of the instantaneous particle positions at different pressures. **Middle row:** Porosity plots from the snapshots of the DPM results at 2, 4, 8 and 16 bar. Only a slice of one cell deep in the middle of the bed is shown. **Bottom row**: Bubble detection results of the snapshots shown in the middle row. The black cells are attributed to bubbles.

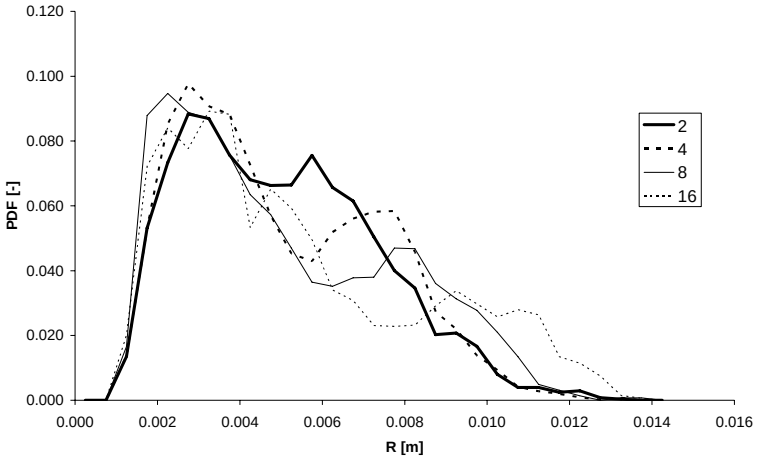

Figure 6: The PDF of the bubble size distribution of all four simulations.

Our bubble detection algorithm experiences difficulties in detecting bubbles at high pressures, due to the less pronounced distinction between the emulsion phase and bubble phase. At 16 bar it is hardly possible to discriminate individual bubbles as can be inferred from Figure 5. In some cases the bubble detection algorithm detects one bubble, which actually consists of a complex bubble-emulsion structure.

The bubble size distribution calculated on basis of the bubble detection results is shown in Figure 6. Bubbles, smaller than 1 mm, are not detectable and are therefore not taken into account. In all cases the mean bubble radius is about 3 mm. At increasing pressure more bubbles larger than 7 mm are observed. Bubbles over 12 mm are hardly seen, since the bed width is 25 mm. From visual inspection of porosity maps of the bed it was found that the bubble size is generally decreasing with pressure. However this trend is not seen in Figure 6, which can be explained as follows. First of all, the minimum bubble size that can be detected is rather small. For this reason, a decrease in bubble size is difficult to detect. In addition it is difficult to detect the bubble at 16 bar, because the bubble-emulsion structure is less distinct in this case.

Based on experiments Davies & Taylor (1950) derived the following expression for the bubble rise velocity:

$$v_b = 0.711\sqrt{d_b g} \tag{7}$$

Chan et al. (1987; Olowson & Almstedt (1990, (1991, (1992; Wiman & Almstedt (1998) reported similar equations for the bubble rise velocity with a slightly modified leading constant.

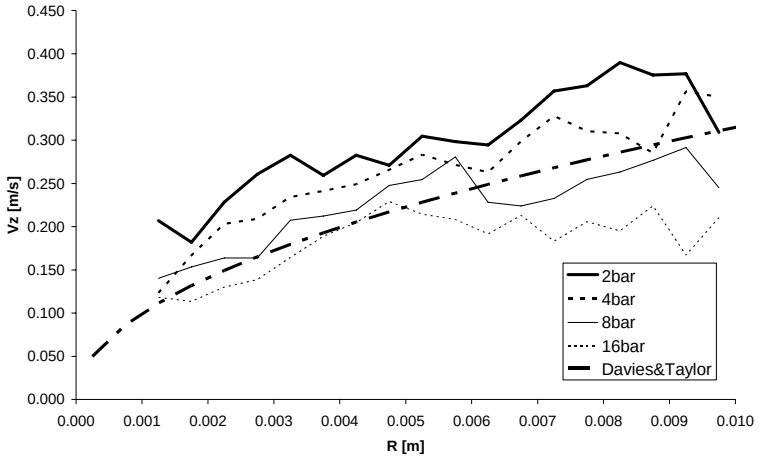

Figure 7: The bubble velocity versus the bubble radius. For reference purposes the Davies and Taylor relation is included.

In Figure 7 the Davies and Taylor relation is shown along with the simulation results. In general the shape of the curves and the magnitude of the bubble velocity are in reasonable accordance with the Davies and Taylor expression. At operating pressures of 2 and 4 bar, the bubble rise velocities exceeded the Davies and Taylor relation. This is probably caused by the upward flow of the emulsion phase surrounding the the bubbles. The effect of the emulsion movement can be eliminated by subtracting the emulsion velocity, as described earlier, yielding a better correspondence with the Davies and Taylor relation, as shown in Figure 8. Especially the results of the 2 bar simulation are very well in accordance.

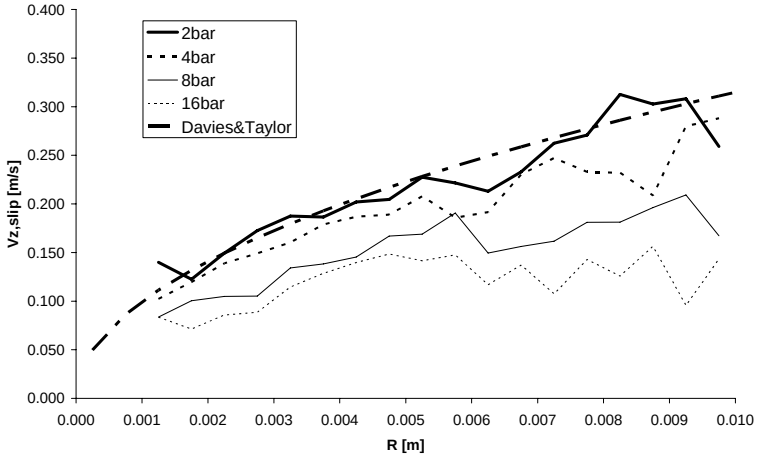

Figure 8: The bubble slip velocity versus the bubble radius. The simulation results are compared with the Davies and Taylor relation.

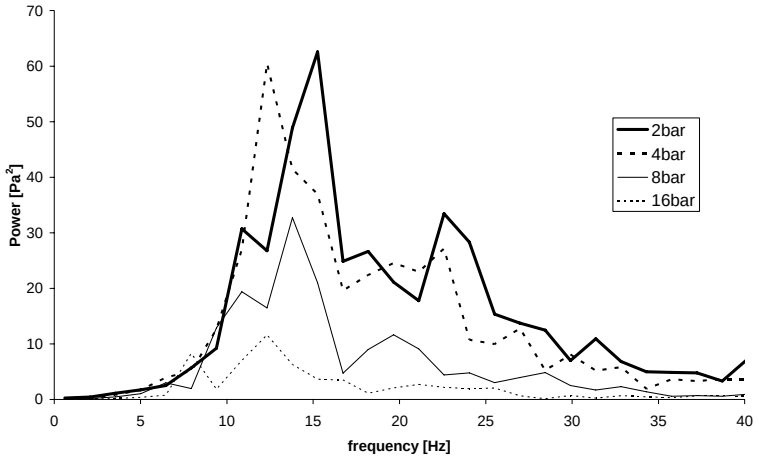

Figure 9: Power spectra of the pressure drop fluctuations of four simulations at operating pressures of 2, 4, 8 and 16 bar.

Finally, we applied a spectral analysis to the bed pressure drop signal, the results of which are shown in Figure 9. We see that the power of the spectrum decreases with increasing pressure. This implies that the pressure drop fluctuations are reduced with increasing pressure, which is a result of the smaller bubble size and reduced heterogeneity of the system.
Furthermore it is observed that the main peaks tend to shift to lower frequencies as the pressure is increased. This suggests that the frequency of bubbles passing through the bed is lower. In order to check this hypothesis, the mean frequency resulting from the spectral analysis is compared with the bubble passage frequency obtained from the bubble detection method (see Table 3).
In the bubble detection algorithm the bubble passage frequency was determined by counting the number of bubbles passing a virtual plane at a height of 0.03 m. This height was chosen since it is in the middle of the bed, no new bubbles are formed at this height and hardly any bubbles collapse.

While the shape of the spectrum is not changing that much, the bubble passage frequency measured with the bubble detection algorithm gradually decreases with pressure. This decrease is especially important between 4 and 8 bar.

The trend seen in the bubble detection algorithm is similar to the average frequency peak from the bubble passage spectrum, but the values differ, especially for the case with operating pressure of 8 and 16 bar.

Operating pressure	Bubble passage frequency	
	Bubble detection algorithm	Spectral analysis
2 bar	22.9 Hz	21.1 Hz
4 bar	20.0 Hz	19.3 Hz
8 bar	14.3 Hz	18.1 Hz
16 bar	12.3 Hz	16.8 Hz

Table 3: Comparison of the bubble passage frequency calculated from the bubble detection algorithm results and the average frequency of the spectral analysis.

Figure 10: Snapshot of the bed porosity in the case where two bubbles are present. The lower bubble sticks to the wall and is much more asymmetric than the bubble in the core of the bed.

Discussion

The results presented in the previous section are subject to some analysis difficulties, leading to some uncertainties in the obtained results. In this section we will discuss some of the aspects related to the choices made in the bubble detection algorithm, the applied bed dimensions and the interpretation of bubble sizes near the wall and at elevated pressures.

In this work, the dimensions of the simulated fluidized bed are rather limited, i.e. $0.025 \times 0.025 \times 0.1$ m^3. The reason that a relatively small bed was used is of a practical nature; due to the high number of particles in the system (i.e. $2.86 \cdot 10^5$) the computation time for one discrete particle simulation of this size is in the order of one month, which is just acceptable. As a result of the dimensional limitations, the predicted bubble sizes are restricted by the size of the bed. Furthermore, wall effects such as a strong particle down flow near the wall will influence the bubble behaviour.

Bubbles near the wall tend to stick to the wall and become strongly asymmetrical as is shown in Figure 10. These bubbles have no interaction with the emulsion phase on the wall. In real industrial scale fluidized beds the walls hardly play any role, since these beds are typically metres wide. We tried to eliminate wall effects on the bubble rise velocity by subtracting the emulsion phase velocity. Furthermore are bubble sizes limited to the bed dimensions and will stop to increase. We plan to simulate larger systems to diminish the wall effects.

As indicated before, the bubble-emulsion structure becomes less distinct with increasing pressure (see Figure 5). One should bear in mind that the ability to distinguish individual bubbles is reduced with increasing pressure.

Conclusions

In this work, we developed a sophisticated bubble detection algorithm. With this algorithm one is able to distinguish bubbles from the emulsion phase in discrete particle simulation results. The bubble detection algorithm was used to investigate the influence of the operating pressure on the fluidization behaviour of a polymeric particles fluidized with air at a constant excess velocity of 0.177 m/s and pressures ranging from 2 to 16 bar.

It was found that the operating pressure significantly influences the fluidization behaviour of polymeric particles. The emulsion phase becomes more dilute with increasing pressure, whereas the bubbles become denser. As a result, the distinction between bubbles and emulsion phase becomes less clear. The applicability of the often used K-L model (Kunii & Levenspiel (1991)), which assumes a separate bubble and emulsion phases, becomes less clear at elevated pressures.

Furthermore, it was found that the bubbles tend to become smaller as the pressure is increased. Finally, at an operating pressure of 2 bar the bubble rise velocity was found to be in very good agreement with the relation of Davies & Taylor (1950). At elevated pressures, the correspondence is less good.

Finally, it was observed that the bubble passage frequency is increasing with increasing pressure, indicating that the bubbles are smaller as pressure is increased. This observation is confirmed by the results of a spectral analysis of the pressure drop fluctuations over the bed.

Based on the findings in this work, one could adapt the Kunni and Levenspiel model porosity increase in the emulsion phase and a porosity decrease in the bubble phase. However since the distinction is not very clear such a model would be susceptible to large uncertainties. The formulation of a fluid bed model at elevated pressures is still an open question, which will be the subject of future work.

References

Bokkers, G.A., van Sint Annaland, M., & Kuipers, J.A.M. (2004). Mixing and segregation in a bidisperse gas-solid fluidised bed: A numerical and experimental study. *Powder Technology*, 140(3), 176-186.

Chan, I.H., Sishtla, C., & Knowlton, T.M. (1987). The effect of pressure on bubble parameters in gas-fluidized beds. *Powder Technology*, 53(3), 217-235.

Chitester, D.C., et al. (1984). Characteristics of fluidization at high pressure. *Chemical Engineering Science*, 39(2), 253-261.

Davies, R.M. & Taylor, G.I. (1950). The mechanics of large bubblies rising through extended luquid in tubes. *Proceedings of the Royal Society of London. Series A*, 200(375-390).

Ergun, S. (1952). Fluid flow rhrough packed columns. *Chemical Engineering Progress*, 48, 89-94.

Hoomans, B.P.B., et al. (1996). Discrete particle simulation of bubble and slug formation in a two-dimensional gas-fluidised bed: A hard-sphere approach. *Chemical Engineering Science*, 51(1), 99-118.

Kharaz, A.H., Gorham, D.A., & Salman, A.D. (1999). Accurate measurement of particle impact parameters. *Measurement Science and Technology*, 10(1), 31.

Koch, D.L. & Hill, R.J. (2001). Inertial effects in suspension and porous-media flows. *Annual Review of Fluid Mechanics*, 33(1), 619-647.

Kunii, D. & Levenspiel, O. (1991). *Fluidization engeneering*. Boston, London, Singapore, Sydney, Toronto, Wellington: Butterwirth-Heinemann.

Laverman, J.A. (2006). Private communication.

Li, J. & Kuipers, J.A.M. (2005). On the origin of heterogeneous structure in dense gas-solid flows. *Chemical Engineering Science*, 60(5), 1251-1265.

Link, J.M., et al. (2005). Flow regimes in a spout-fluid bed: A combined experimental and simulation study. *Chemical Engineering Science*, 60(13), 3425-3442.

Olowson, P.A. & Almstedt, A.E. (1990). Influence of pressure and fluidization velocity on the bubble behaviour and gas flow distribution in a fluidized bed. *Chemical Engineering Science*, 45(7), 1733-1741.

Olowson, P.A. & Almstedt, A.E. (1991). Influence of pressure on the minimum fluidization velocity. *Chemical Engineering Science*, 46(2), 637-640.

Olowson, P.A. & Almstedt, A.E. (1992). Hydrodynamics of a bubbling fluidized bed: Influence of pressure and fluidization velocity in terms of drag force. *Chemical Engineering Science*, 47(2), 357-366.

Sidorenko, I. & Rhodes, M.J. (2004). Influence of pressure on fluidization properties. *Powder Technology*, 141(1-2), 137-154.

Wen, Y.C. & Yu, Y.H. (1966). Mechanics of fluidization. *Chemical Engineering Progress Symposium*, 62, 100-111.

Wiman, J. & Almstedt, A.E. (1998). Influence of pressure, fluidization velocity and particle size on the hydrodynamics of a freely bubbling fluidized bed. *Chemical Engineering Science*, 53(12), 2167-2176.

Ye, M., van der Hoef, M.A., & Kuipers, J.A.M. (2005). The effects of particle and gas properties on the fluidization of geldart a particles. *Chemical Engineering Science*, 60(16), 4567-4580.